Benjamin Männel, Henryk Dobslaw, Robert Dill, Susanne Glaser, Kyriakos Balidakis, Maik Thomas, Harald Schuh

Correcting surface loading at the observation level: impact on global GNSS and VLBI station networks

Journal article | **Accepted manuscript (Postprint)**
This version is available at https://doi.org/10.14279/depositonce-11879

This is a post-peer-review, pre-copyedit version of an article published in Journal of Geodesy. The final authenticated version is available online at: http://dx.doi.org/10.1007/s00190-019-01298-y

Männel, B., Dobslaw, H., Dill, R., Glaser, S., Balidakis, K., Thomas, M., & Schuh, H. (2019). Correcting surface loading at the observation level: impact on global GNSS and VLBI station networks. Journal of Geodesy, 93(10), 2003–2017. https://doi.org/10.1007/s00190-019-01298-y

Journal of Geodesy manuscript No.
(will be inserted by the editor)

Correcting surface loading at the observation level: Impact on global GNSS and VLBI station networks

Benjamin Männel · Henryk Dobslaw · Robert Dill · Susanne Glaser · Kyriakos Balidakis · Maik Thomas · Harald Schuh

Received: date / Accepted: date

Abstract Time-dependent mass variations of the near-surface geophysical fluids in atmosphere, oceans and the continental hydrosphere lead to systematic and significant load-induced deformations of the Earth's crust. The Earth System Modelling group of Deutsches GeoForschungsZentrum (ESMGFZ) provides vertical and horizontal surface deformations based on numerical models of the global geophysical fluids in atmosphere, oceans and the continental hydrosphere with a spatial resolution of 0.5° and a temporal sampling of down to three hours (Dill and Dobslaw, 2013). The assessment of conventionally – i.e. without consideration of non-tidal loading models – processed global GNSS datasets reveals that large parts of the residual station coordinates are indeed related to surface loading effects. Residuals explained by the models often have a pronounced annual component, but variability at other periodicities also contributes to generally high correlations for seven-day averages. More than ten years of observations from about 400 GNSS and 33 VLBI stations were specifically reprocessed for this study to incorporate non-tidal loading correction models at the observation level. Comparisons with the corresponding conventional processing schemes indicate that the coordinate repeatabilities and residual annual amplitudes decrease by up to 13 mm and 7 mm, respectively, when ESMGFZ's loading models are applied. In addition, the standard deviation of the daily estimated vertical coordinate is reduced by up to 6.8 mm. The network solutions also allow for an assessment of surface loading effects on GNSS satellite orbits, resulting in radial translations of up to 4 mm and Earth orientation parameters (EOP). In particular the VLBI-based EOP estimates are critically susceptible to surface loading effects, with root-mean-squared differences reaching of up to 0.2 mas for polar motion, and 10 µs for UT1-UTC.

B. Männel · H. Dobslaw · R. Dill · S. Glaser · K. Balidakis · M. Thomas · H. Schuh
Deutsches GeoForschungsZentrum GFZ, Telegrafenberg, 14473 Potsdam, Germany
E-mail: benjamin.maennel@gfz-potsdam.de

M. Thomas
Institute of Meteorology, Freie Universität Berlin, Carl-Heinrich-Becker-Weg 6-10, 12165 Berlin, Germany

H. Schuh
Institute of Geodesy and Geoinformation Science, Technische Universität Berlin, Strasse des 17. Juni 135, 10623 Berlin, Germany

Keywords GNSS · VLBI · non-tidal surface loading · GNSS orbits · polar motion

1 Introduction

The redistribution of mass within the interactively coupled System Earth can be conveniently separated in periodic and non-periodic components. The former part is typically associated with tidal phenomena in solid Earth, oceans and atmosphere, whereas the latter is caused by transient dynamics in atmosphere, oceans and the terrestrial branch of the global water cycle. According to geophysical loading theory (e.g., Lambeck, 1988), each mass anomaly at the surface of the solid Earth causes a deformation and an associated change in the Earth's gravity field, its orientation, and – most important for this study – the geometry of the crust. The effect of non-tidal atmospheric loading on VLBI-measurements was already investigated by Rabbel and Schuh (1986) and it was shown by Schuh and Möhlmann (1989) that tidal ocean loading corrections significantly reduce the post-fit RMS and the baseline length repeatability. For GNSS, Dong et al (2002) found that about

40 % of annual height variations are explained by seasonal water mass re-distributions. In addition, surface loading affects also GPS-based horizontal station velocities (Blewitt and Lavallee, 2002). Consequently, surface loading should be considered for high-precision space geodesy especially in the view of the accuracy goals of the Global Geodetic Observing System (GGOS) that aim at 1 mm coordinate accuracy and 0.1 mm/a stability. The International Earth Rotation and Reference Systems Service (IERS) Conventions 2010 (Petit and Luzum, 2010) recommend that atmospheric and ocean tidal loading should be corrected at the observation level. For non-tidal loading, no such recommendation was made in the 2010 conventions, which might be related to the limited availability of non-tidal background models available at that time.

In more recent years, several authors assessed the impact of non-tidal loading corrections on space geodetic results. Tregoning and van Dam (2005) studied the impact of correcting non-tidal atmospheric loading at the observation level in GPS data analysis. They derived corresponding corrections from global surface pressure estimates at high temporal resolution reduced for effects of atmospheric tides. Overall, they found decreased WRMS values for the height component of about 77 % of their set of globally distributed stations. Around the same time, Petrov and Boy (2004) developed an alternative atmospheric pressure loading model and found admittance factors close to unity for VLBI data. Böhm et al (2009) demonstrated that in VLBI the atmopsheric loading corrections have to be rigorously applied at the observation level to obtain the best possible results and to avoid systematic biases in the station heights and other estimated parameters. Dach et al (2011) applied a similar model to a global GPS network and found a 20 % improvement in GPS station coordinate repeatabilities. van Dam et al (2012) applied non-tidal ocean loading to the coordinates provided in MIT's reprocessed GPS solution `mi1`. A reduction in the scatter was found for 65 % of the investigated stations with a major (i.e., 80 %) contribution of the annual signal of the ocean bottom pressure variability. Roggenbuck et al (2015) studied the impact of non-tidal surface loading concurrently applied to global GNSS, VLBI, and SLR analyses and found, for example, for 93 % of the considered GNSS stations reductions in the height RMS of up to 50 %. In addition, they reported a substantial decrease in the seasonal variations in the derived geocenter estimates. The impact of atmospheric and oceanic loading was also discussed by Männel and Rothacher (2017) in the framework of consistently processed ground and space-based GNSS observations. Several authors discussed the impact on regional networks usually by applying high-resolution models. Williams and Penna (2011) reported RMS reductions of 20 % for stations around the North Sea when applying non-tidal loading corrections. Similar conclusions were also drawn by Nordman et al (2015), who achieved variance reductions of 56 %, 30 %, and 16 % in east, north, and up direction for GNSS stations in the Baltic Sea region.

The accessibility of model-based non-tidal global surface loading deformations has been much improved over the last decade. The *International Mass Loading Service* (`http://massloading.net`) offers products based on a wide range of NASA models (Petrov and Boy, 2004). The EOST Loading Service of University of Strasbourg (http://loading.u-strasbg.fr) provides surface loading deformations based on a range of models developed in Europe (Gegout et al, 2010). The Earth System Modelling group of Deutsches GeoForschungsZentrum (ESMGFZ) in Potsdam (`http://isdc.gfz-potsdm.de/esmdata/loading`) also provides surface loading data based on models of atmosphere, oceans and the terrestrial hydrosphere (Dill and Dobslaw, 2013). In the present manuscript we thus attempt to evaluate the impact of this state-of-the-art model data set of non-tidal surface deformation on specifically reprocessed global datasets of GNSS and VLBI. After a brief description of the ESMGFZ loading models (Sect. 2) and a short introduction of the different GNSS and VLBI processing strategies applied in this study (Sect. 3), we correlate coordinate timeseries of conventionally processed global GNSS data (Sect. 4) with the ESMGFZ loading models in order to underline the dominance of atmosphere-hydrosphere deformation signatures in present-day GNSS timeseries. Subsequently, the loading models are introduced as background models at the observation level for both GNSS and VLBI, and the consequences for the resulting coordinate repeatabilities are studied (Sect. 5). Attention is also paid in this section to consequences of the applied loading models on derived quantities as GNSS satellite orbits and Earth Orientation Parameters. The paper closes with a brief summary and some conclusions in Sect. 6.

2 GFZ Earth System Model (ESM) surface loading models

The Earth System Modelling group of Deutsches GeoForschungsZentrum (ESMGFZ) in Potsdam, Germany, is routinely calculating elastic surface deformations caused by non-tidal loadings in atmosphere, ocean, and continental hydrosphere calculated by a patched Green's function approach (Farrell, 1972) as described in Dill

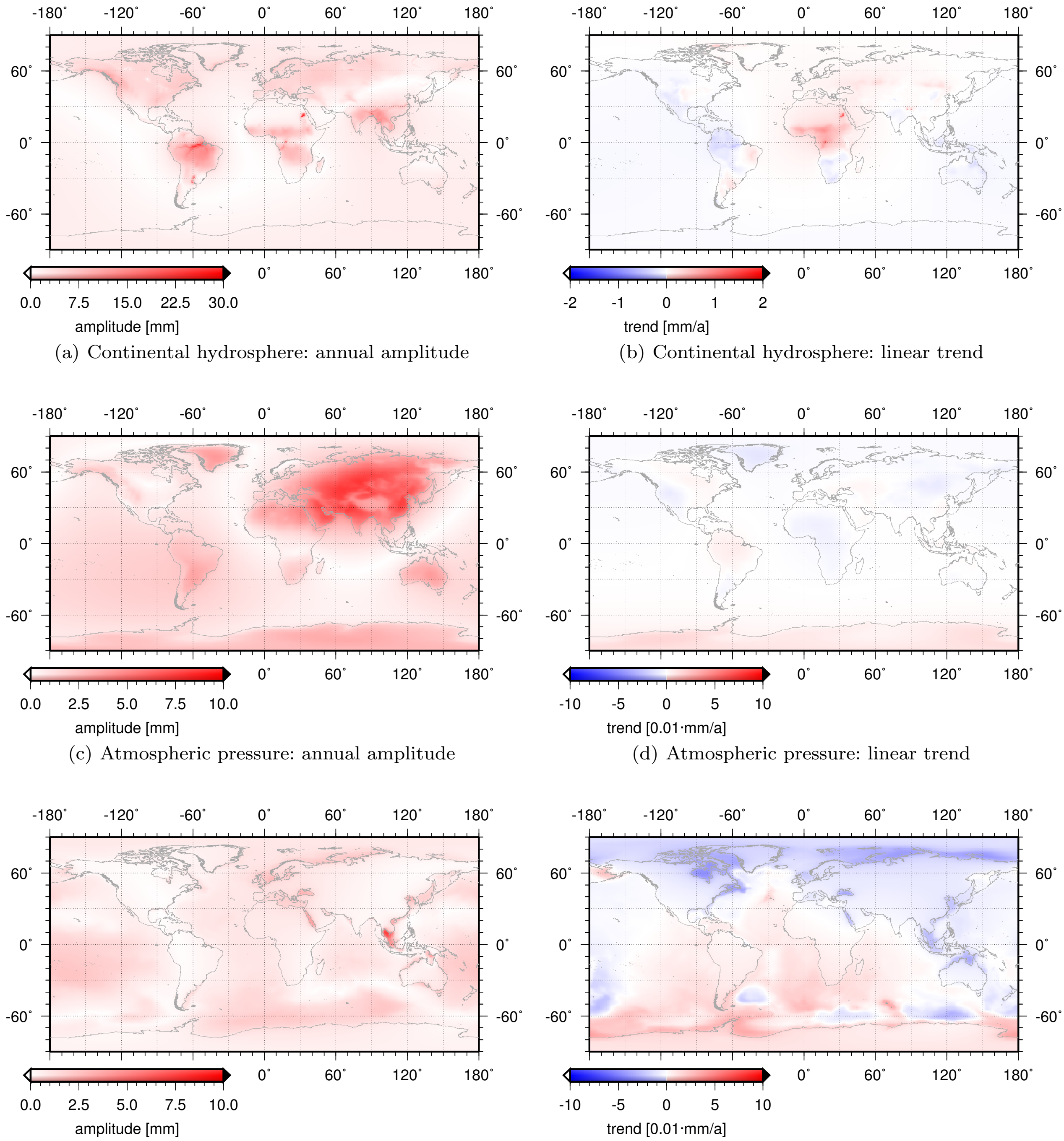

(a) Continental hydrosphere: annual amplitude

(b) Continental hydrosphere: linear trend

(c) Atmospheric pressure: annual amplitude

(d) Atmospheric pressure: linear trend

(e) Ocean loading: annual amplitude

(f) Ocean loading: linear trend

Fig. 1 Annual signals and long-term trends in terrestrial water storage, atmospheric pressure, and ocean loading as given in the ESMGFZ model; computed between 1979.0 and 2018.0 as 0.5° × 0.5° grid; please note the different scales for continental hydrosphere and Dobslaw (2013). The calculations are performed in the spatial domain on 0.125° × 0.125° global grids in the near-field (0° - 3.5°) and on 2.0° × 2.0° grids in the far-field (3.5° - 180°) by using mass distributions provided by the deterministic numerical weather prediction model of the European Centre for Medium-range Weather Forecasts (ECMWF), the Max-Planck-Institute for Meteorology Ocean Model (MPIOM, Jungclaus et al, 2013), and the Land Surface Discharge Model (LSDM, Dill, 2008). The re-mapping applied to all datasets to arrive at the 0.125° resolution required for the near-field calculations is described in Dill et al (2018). Based on global load Love numbers taken from the elastic Earth model ak135 (Kennett et al, 1995), the surface deformations are provided in two different frames, namely center of the Earth's figure (CF) and center of Earth's mass (CM). Atmospheric, oceanic, and hydrospheric loading surface deformations in north, east, and up are provided with a spatial resolution of 0.5° and a temporal sampling of three hours for atmosphere and ocean, and 24 h for the continental hydrosphere, (Dill and Dobslaw, 2013). For operational users, the ESMGFZ products are updated daily at 10:00 UTC, and even provide forecasts for up to six days into the future based on the routine numerical weather forecasts issued by ECMWF. In view of the GGOS consistency goals, it should be mentioned that ESMGFZ is also providing background models for satellite gravimetry (AOD1B; Dobslaw et al, 2017) and Earth orientation excitation functions (EAM; Dobslaw et al, 2010) that are each based on identical mass distributions as the surface loading deformations. Figure 1 shows the deformations in vertical direction characterized by their annual amplitude (figures *a, c, e*) and by their secular trend (figures *b, d, f*) for non-tidal continental hydrosphere (*top*), atmospheric pressure (*middle*), and ocean loading (*bottom*). Both quantities, the annual amplitude A_i and the linear trend b_1, are determined by applying a least squares fit:

$$C(t) = \sum_{i=1}^{n} A_i \sin\left(\frac{2\pi}{P_i}(t - t_0) + \phi_i\right) + b_0 + b_1(t - t_0). \quad (1)$$

In Eqn. 1, the annual period is indicated by P_i, the time epoch t_0 is given by January 1st. Parameters ϕ_i and b_0 specify the phase shifts and the coordinate at reference epoch J2000.0, respectively. Annual amplitudes (see left part of Figure 1) reach more than 30 mm for the continental hydrosphere, highlighting the major river basins like Amazon, Parana, Congo, Yangtze, and Ganges. Large scale variation patterns are also visible in North America, Eurasia, and Africa with annual amplitudes of up to 5 mm. Atmospheric pressure loading exceeds 10 mm particularly in regions of long-term stable air pressure regimes like in the interior of Eurasia, Antarctica, and Greenland. Non-tidal ocean loading reaches amplitudes of 10 mm only in some semi-enclosed seas in Southeast Asia. The right column of Figure 1 shows regional long-term trends in the vertical deformations. In general, positive trends are associated with decreasing surface loads. Deformations related to atmospheric and ocean loading are always smaller than 0.1 mm/a with, in general, large-scale patterns. Trends in deformations related to continental hydrosphere are substantially larger and more spatially heterogeneous. Significantly positive annual uplift rates of up to 1 mm/a are found for several regions. Most prominent are the positive trends (i.e. decreased loading) in central Africa, South America, and the northwest part of Greenland. Negative trends associated with increased surface loading and associated station subsidence are visible in the Amazon region, Western US, and West Australia. It is worth to be mentioned that also very local effects can create strong trends, as visible for the region of the Lake Nasser in Egypt (Figure 1(b)).

3 GNSS and VLBI data processing

In order to (1) compare the surface deformations given in the models against station coordinate time series as well as to (2) assess potential improvements in e.g. velocity estimation, both global GNSS (actually GPS-only) and VLBI datasets were analyzed. GNSS observations were processed with the GFZ software EPOS.P8 in both network and precise point positioning (PPP) mode. In general, the GNSS processing followed the IERS 2010 Conventions (Petit and Luzum, 2010) and was performed in the ITRF2014 reference frame (Altamimi et al, 2016).

The GNSS network solution was set up similar to the GFZ IGS rapid processing, i.e. including the estimation of orbit and Earth rotation parameters. A network of 156 globally distributed stations was selected with data from the period 2008.0 to 2018.0. For the implications of using a Global Mapping Function when investigating loading effects we refer to Steigenberger et al (2009).

The GNSS PPP-solution comprises in total 484 stations for the time period 2008.8 to 2017.1. Orbit and clock products are taken from a GFZ internal reprocessing effort which was set up similar to the configuration of GFZ official IGS products. However, as the a priori products used in the PPP processing were computed without applying surface loading corrections the effect of surface loading is not fully considered (the impact of surface loading on satellite orbits is discussed in Sect. 5).

Tab. 1 Summary of estimation and processing strategy; entries applicable for more than one solution are specified in merged cells; time span 2008-2018

<table>
<tr><th></th><th>GNSS (PPP solution)</th><th>GNSS (network solution)</th><th>VLBI</th></tr>
<tr><td colspan="4">modeling and a-priori information</td></tr>
<tr><td>observations</td><td colspan="2">ionosphere-linear combination formed by undifferenced GPS observations</td><td>group delays IVS-R1 and R4 sessions</td></tr>
<tr><td>a priori products</td><td colspan="2">orbits, clock corrections, Earth rotation parameters from internal reprocessing</td><td>Earth rotation parameters from IERS C04 14</td></tr>
<tr><td>tropospheric correction</td><td colspan="2">troposphere delays computed with Saastamoinen, mapped with GMF (Böhm et al, 2006)</td><td>troposphere delays computed with Saastamoinen, mapped with PMF</td></tr>
<tr><td>ionospheric correction</td><td colspan="2">1st order effect considered with ionosphere-free linear combination</td><td>X-band observations corrected with S-band</td></tr>
<tr><td>GNSS phase center</td><td colspan="2">igs14_2013.atx applied</td><td>-</td></tr>
<tr><td>clock datum</td><td></td><td>zero-mean condition for satellites and selected stations</td><td></td></tr>
<tr><td>gravity potential</td><td colspan="2">EGM2008</td><td>-</td></tr>
<tr><td>solid Earth tides</td><td colspan="3">according to IERS 2010 Conventions (Petit and Luzum, 2010)</td></tr>
<tr><td>permanent tide</td><td colspan="3">conventional tide free</td></tr>
<tr><td>ocean tide model</td><td colspan="3">FES2004 (Lyard et al, 2006)</td></tr>
<tr><td>ocean loading</td><td colspan="3">tidal: FES2004 (Lyard et al, 2006)</td></tr>
<tr><td>atmospheric loading</td><td colspan="3">tidal: S_1 and S_2 corrections (Ray and Ponte, 2003)</td></tr>
<tr><td>non-tdial loading</td><td>CF-frame</td><td>CM-frame</td><td>CM-frame</td></tr>
<tr><td colspan="4">parametrization</td></tr>
<tr><td>station coordinates</td><td>freely estimated</td><td>NNR to ITRF2014</td><td>NNT, NNR to ITRF2014</td></tr>
<tr><td>troposphere</td><td colspan="2">25 zenith delays; GMF; two gradient pairs per station and day</td><td>25 zenith delays; PMF; five gradient pairs per station and day</td></tr>
<tr><td>GPS orbit modeling</td><td>-</td><td>initial conditions, ECOM2, pulses at 12 h, arc length 24 h</td><td>-</td></tr>
<tr><td>source coordinates</td><td>-</td><td>-</td><td>NNR to ICRF2</td></tr>
<tr><td>Earth rotation</td><td>-</td><td>rotation pole coordinates and UT1 for 24 h intervals</td><td>rotation pole coordinates and UT1 for 24 h intervals</td></tr>
<tr><td>receiver clock</td><td colspan="2">pre-eliminated every epoch</td><td>2nd degree clock polynomial</td></tr>
<tr><td>GNSS ambiguities</td><td>float solution</td><td>ambiguity fixing</td><td>-</td></tr>
</table>

Therefore, PPP results are used only to compare GNSS coordinate time series against the deformations given in the models. More details on the processing and the estimated parameters can be found in Table 1.

VLBI group delays observed by 33 radio telescopes in IVS-R1 and R4 sessions between 2006.0 and 2018.0 were processed using the VieVs@GFZ software (Nilsson et al, 2015). The processing is consistent with the IERS 2010 Conventions (Petit and Luzum, 2010), however, the Potsdam mapping function (PMF, Zus et al, 2014 and Balidakis et al, 2018) was used. The required no-net-translation and no-net-rotation conditions were applied to 30 selected datum stations. The VLBI station coordinate time series were created similar to the GNSS time series, i.e., from session-wise 24 h solutions.

Based on the estimated daily or session-wise station coordinates time series were formed. GNSS antenna changes as reported in the IGS site log files as well as strong earthquakes (NOAA Earthquake Database[1]) were considered as well as additional jumps detected while forming the time series. Annual signals and linear trends (i.e., station velocities) were estimated using Eqn. 1.

4 Comparison between GNSS station coordinate time series and surface loading models

The first objective of this paper is a comparison between deformations provided by the surface loading models and variations in the GNSS-determined station height

[1] `https://www.ngdc.noaa.gov/nndc/struts/form?t=101650s=1d=1`, accessed June 2019

coordinates. The overall goal is to check whether the corrections are reasonable for being applied at the observation level. Consequently, the GNSS solutions discussed within this section have been derived without correcting for the modeled surface deformation. This section is divided into three parts. Firstly, the comparison is done exemplarily for a region with large loading effects, whereas the second and third part focus on annual signals and correlations as observed by a global GNSS network. To analyze the correlation in more detail, also time series of individual stations are discussed.

4.1 Monitoring hydrological loading in the Amazon basin

Located in the Amazon basin, one can expect large periodic variation in the GNSS coordinate time series of Porto Velho (POVE, Brazil) related to large water storage variations and large river channel loads. As already pointed out by Dill and Dobslaw (2013) the region of Porto Velho is affected by the large scale deformations of the Amazon river channel located several hundred kilometers away and by the near-field loading of the Madeira river which is the biggest tributary to the Amazon. Figure 2 shows the height coordinate of POVE (*gray*) and the site displacement as given in the ESM hydrological loading files (*black*). Two earthquakes affected the station in 2014 (Iquique, $M_w = 8.2$) as well as in 2015 (Peru-Brazil border region, $M_w = 7.6$). According to the IGS site log, a third discontinuity occurred in July 2015 as the GNSS antenna was replaced. Overall, a good agreement is found between surface deformations given in the loading model and observed station displacements. In both solutions, station displacements follow a strong annual period with peak-to-peak variations of 35-45 mm. This amplitude is large compared to most of the IGS stations but considerably smaller than the 50-75 mm by Bevis et al (2005) reported for the GPS station MANA located in Manaus close to the riverbanks of Rio Negro and Amazon. The annual signals for POVE are characterized with their amplitude and phase in Table 2. The agreement between deformations from GNSS and from the model is good with 14 days difference in phase and 2 mm difference in amplitude. Hydrological loading will explain 80 % of the amplitude observed in the GNSS solution for POVE. In addition, Table 2 contains values for the station in Brasilia (BRAZ), showing also a good agreement with offsets of 3 mm in amplitude and 15 days in phase. Based on the individual daily coordinates cross-correlation was performed which confirms the phase differences by providing time lags τ of 14 days for both sites and correlation factors of 0.89 and 0.75 for POVE and BRAZ, respectively. Based on an earlier model configuration, Dill and Dobslaw (2013) predicted the loading signal to be 21 days earlier than the coordinate signal but found a similar correlation coefficient of 0.80 for POVE when contrasted against freely available GNSS coordinate solutions of that time.

4.2 Comparison of annual amplitudes and phases

By extending this analysis to the whole globe, annual amplitudes and phase shifts were estimated for all 484 stations contained in the PPP processing. Similar to POVE, also other stations have been subject to earthquakes and antenna changes, consequently, we split the 484 time series into in total 1198 segments. To derive reliable annual signals, time series shorter than 900 days (2.5 years) were excluded from the following investigations. It is obvious that some stations might have two or even more time series longer than 900 days whereas few stations were processed for periods shorter than 900 days. Figure 3 shows the amplitudes and phases derived for the remaining 437 station height coordinate time series as well as the corresponding values derived from the modelled hydrospheric deformations given in the center-of-figure frame. We computed agreement factors for the amplitudes as

$$C_A = \frac{A_{model}}{A_{coordinate}}, \tag{2}$$

and for the phase as

$$C_P = 1 - \frac{P_{model} - P_{coordinate}}{180}, \tag{3}$$

color-coded in Figure 3 with the phase agreement shown in the amplitude plot and vice versa. In most cases, the amplitudes in the coordinate time series are larger than those obtained from the model, and amplitudes agree within ±10 % for only 3.1 % of the time series considered. An agreement of at least 40 % as stated by Dong et al (2002) is found for 45 % of the time series. However, it is clear that GNSS time series are affected not only by the terrestrial water storage loading but also by other loadings, monument stability and local deformations. In addition, technique-specific errors might propagate into the annual amplitudes, such as draconitic orbit errors with their close-to annual periods. Looking on the color-coded phase agreement, we generally note increased phase agreement for larger amplitudes. For the phase shifts, however, larger differences are visible. Phases agree within ±33 % (corresponding to two months) for 64.6 % of the time series. Corresponding to the better phase agreement for larger amplitudes, we note larger amplitude differences mainly for stations with significant phase shifts.

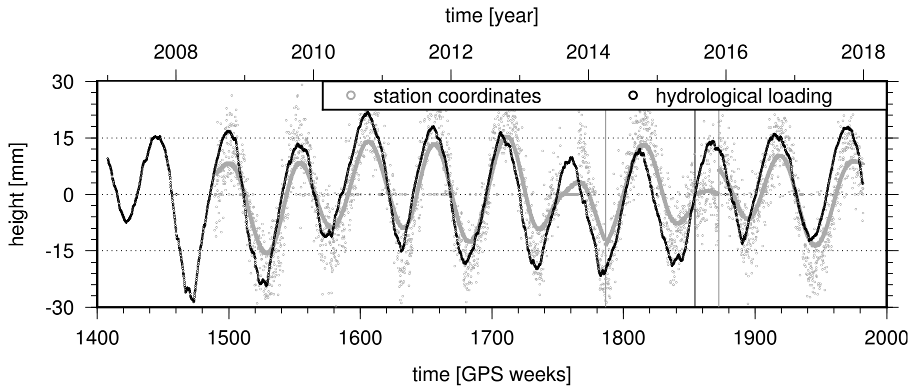

Fig. 2 Height deformation time series for Porto Velho (Brazil, IGS station POVE): coordinate variations (*gray*, including Gaussian filtered line of width 365 days) and surface deformations due to continental hydrosphere (*black*); vertical lines indicate earthquakes close to Iquique (2014) and the Peru-Brazil border region (2015) and an antenna change in July 2015, respectively

Tab. 2 Annual signal in the height component for Porto Velho (POVE) and Brasilia (BRAZ) (annual signals are computed according to Eq. 1), correlation specified as time lag and correlation factor; time span: 2008.0-2014.25 (POVE), 2008.0-2012.7 (BRAZ)

	hydrological model		station height coordinate		correlation	
	amplitude [mm]	phase [°]	amplitude [mm]	phase [°]	shift [d]	coefficient [-]
POVE (Porto Velho, Brazil)	15.8±0.1	180.8±0.4	17.7±0.2	167±0.7	14	0.89
BRAZ (Brazil, Brasilia)	8.1±0.1	182.8±0.5	11.1±0.2	167±1.2	14	0.75

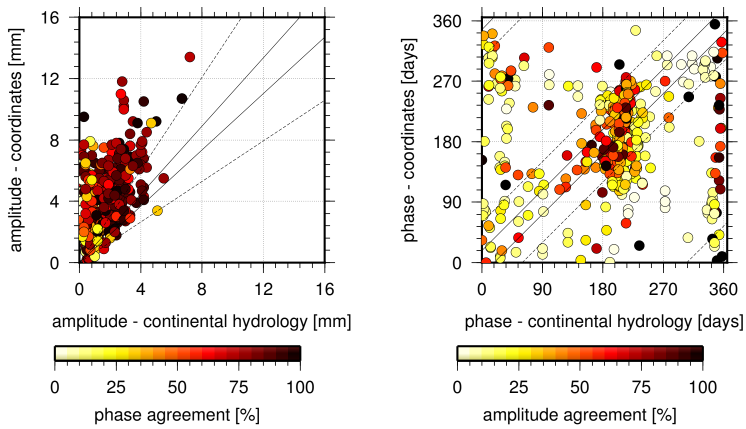

(a) Amplitude with color-coded phase agreement (b) Phase with color-coded amplitude agreement

Fig. 3 Annual signal of GNSS coordinate time series (PPP) and continental hydrosphere in up direction; agreement within ±10% (*solid*) and ±33% (*dashed*)

4.3 Correlations

Figure 4 shows correlation factors computed between station height time series and the vertical deformations provided in the models of atmosphere, ocean, and continental hydrosphere. In order to reduce the remaining day-to-day variation in the GNSS time series a seven day moving average was introduced here instead of the daily coordinates when computing the correlation coefficients. Overall, correlation factors larger than 0.5 are visible for stations located in Europe, South America, and North America with largest correlations in the Amazon region. For island and coastal stations weaker correlations are visible. This was already noticed by Dill and Dobslaw (2013) who mentioned the high variability

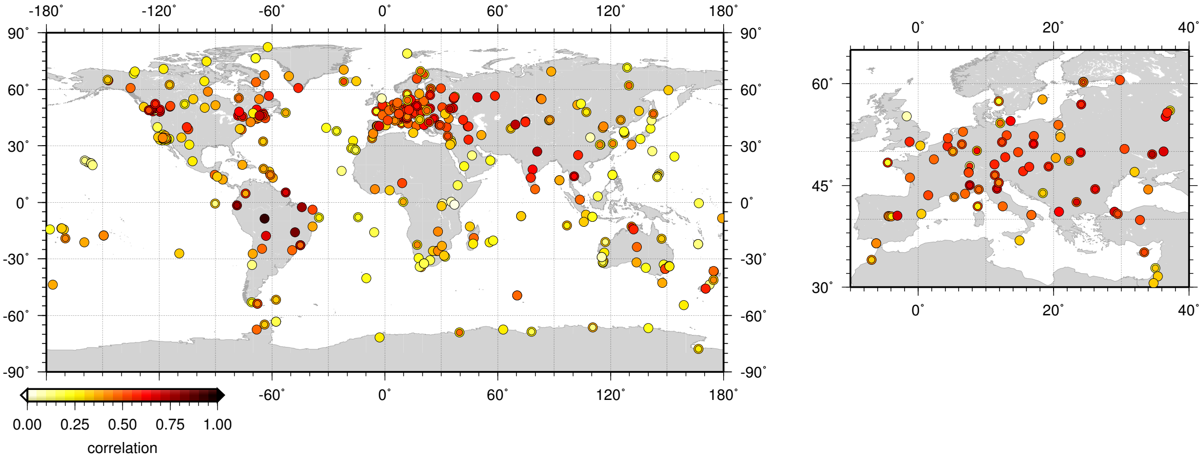

Fig. 4 Correlation between GNSS coordinate time series (PPP, seven-day averages, trends removed) and sum of non-tidal loading (atmosphere + ocean + continental hydrosphere); detailed map for Europe on the right

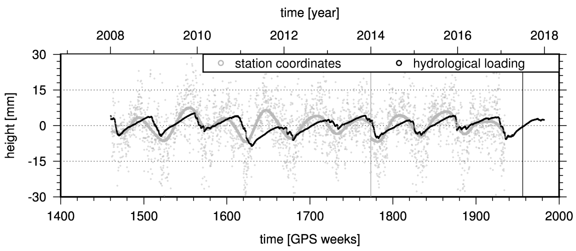

(a) DARW (Darwin, Australia)

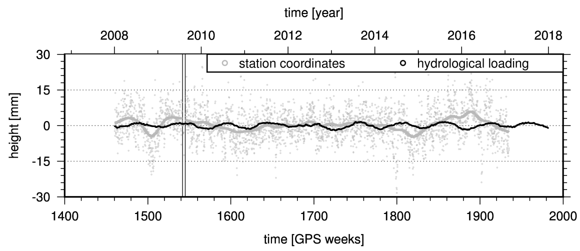

(b) MORP (Morpeth, United Kingdom)

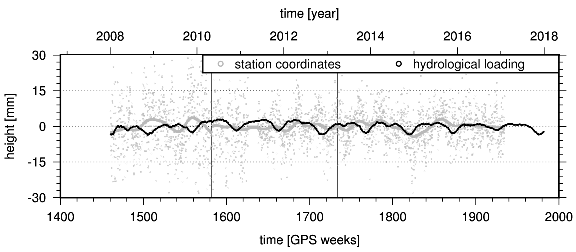

(c) NKLG (N'Koltang, Gabon)

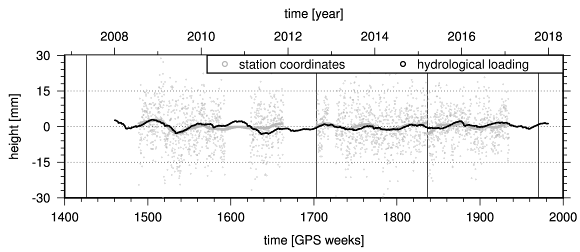

(d) RECF (Recife, Brazil)

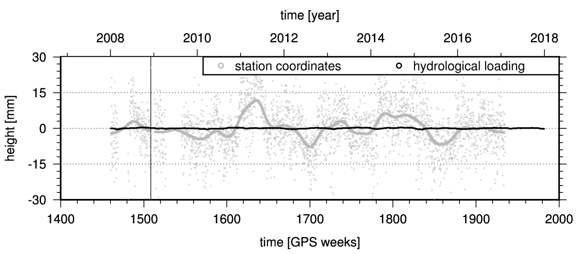

(e) REUN (La Tampon, France)

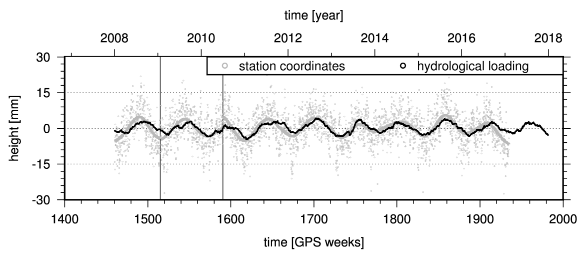

(f) WTZR (Wettzell, Germany)

Fig. 5 Comparison of deformations caused by continental hydrosphere (*black*) and GNSS station height coordinates (without applied models, *gray*, including Gaussian filtered line of width 365 days); trends are subtracted; vertical lines indicate antenna changes of GNSS height coordinates for those stations which is not reflected in the global models.

Based on the global comparison, six individual sites were selected for a more detailed discussion by showing the station height coordinates and the modelled deformation caused by terrestrial water storage (Figure 5). The general noise level for daily PPP-derived station height coordinates reach a level of around 2 cm. Hydrological loadings intensified by human-controlled water management causes a saw tooth deformation pattern for station DARW (Darwin, Northern Territory, Australia). As described by Dill and Dobslaw (2013) the human induced water storage, for example, at the Darwin River Dam is not considered in the models. Figure 5(a) shows strongly increased loading during winter months and slower relaxation between spring and autumn (*black curve*). The associated deformation reaches 6 mm in height. Estimated annual (harmonic) signals cannot represent this behavior adequately, however, the daily coordinates follow the load-induced deformation quite well (*gray points*). This is confirmed by correlation factors of 0.44 and 0.64 before 2014 and afterwards, respectively. For MORP (Morpeth, United Kingdom), a station close to the coast line of the North Sea, deformations are small but systematic with positive amplitudes of around 2 mm during summer. However, the station coordinates show a different behavior almost without annual or seasonal signals between 2010 and 2014. Since late 2014 a systematic height signal is visible. For the IGS station NKLG (N'Koltang, Gabon) located close to the Atlantic coast, hydrological-driven deformations reach up to 6 mm with annual and semi-annual signals. In general, the coordinates follow this pattern but partly with very long build-up times of around three months. According to Nahmani et al (2012), this station is affected by the West African Monsoon region. Consequently, precipitation is abundant between November and March with a short dry season between June and September. This pattern is well reflected by the black curve in Figure 5(c). For RECF (Recife, Brazil), located also closely to the coast, annual signals in the continental water storage reach 3 mm. Due to the coordinate noise a small correlation factor of 0.22 can be determined, however, the phases agree by around 7° (HYDL: 115°, coordinate: 108°). REUN, located at the island La Reunion, France, is almost unaffected by non-tidal loading (models provide vertical deformations below 2 mm). However, the coordinates show significant deformations of up to 10 mm which are most probably related to loading independent local or geodynamical processes. A similar height time series was presented by Peltier et al (2015). For WTZR (Wettzell, Germany) again a strong annual deformation pattern can be observed with amplitudes of up to 7 mm during summer. In general, the station coordinates follow almost immediately the loading signal (phase difference). A correlation factor of 0.60 and a time shift of 17 days can be found.

The examples discussed within this section show that surface deformations due to non-tidal loading cannot be expressed accurately by a sinusoidal annual signal nor by a set of two to three harmonic functions which covers seasonal periods. Depending on the local environment, deformations might change very rapidly for one season and slowly for others. Corresponding GNSS coordinate time series follow these modelled surface deformations in many instances despite the fact that they might be affected also by other local effects. Overall, we found good agreement between the global displacement models and the GNSS coordinate time series.

5 Impact of surface loading deformations on GNSS and VLBI solutions

Within this section the impact of applying the surface loading deformations on the estimated parameters, station coordinates (Sect. 5.1), Earth rotation parameters and satellite orbits (Sect. 5.2), is discussed. These investigations consider only the GNSS network solution as the PPP solutions discussed above were computed with conventional satellite orbits, i.e., orbits without applied corrections. Regarding the station coordinates the analysis focuses on reductions of (1) standard deviation of the estimated coordinates, (2) annual amplitudes and (3) height coordinate repeatabilities. The GNSS network solution with 156 stations provides 178 segments which are longer than 900 days.

5.1 Station Coordinates

In order to assess the impact of applying loading corrections at the observation level we assessed first the estimated station height coordinate. Without any trend reduction, one could expect smaller variations over time when correcting for surface loading. Figure 6 shows a histogram of the differences between the corresponding standard deviations. We found an improvement (i.e., smaller standard deviations) for around 78 % of the assessed segments. The largest improvement is observed for the station POVE (-6.8 mm). For around 3 % of the considered stations namely HOFN (Iceland, +0.6 mm), TRO1 (Norway, +0.8 mm), and YELL (Canada, +0.7 mm) an increase of larger than 0.5 mm was derived. The majority of stations with increased standard deviations are

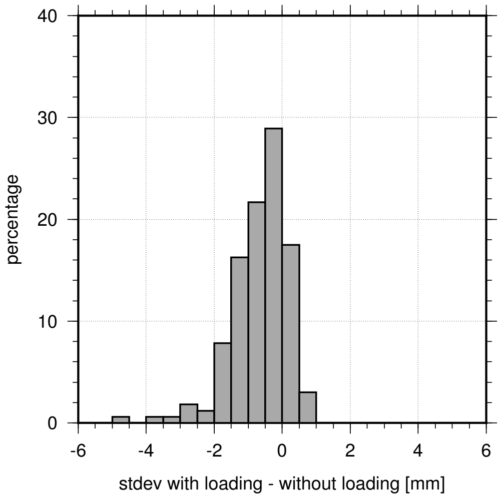

Fig. 6 Impact on standard deviation of raw station height; GNSS network solution; differences *with - without applied models* are shown

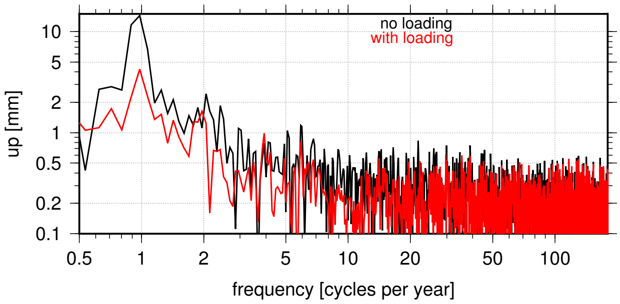

Fig. 7 Spectra of GNSS-derived height coordinate time series with and without applied surface loading corrections; Porto Velho (Brazil, IGS station POVE)

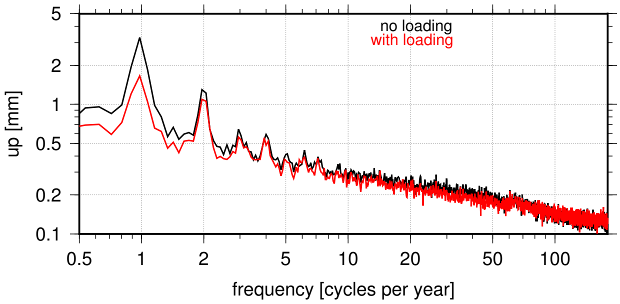

Fig. 8 Spectra of GNSS-derived height coordinate time series with and without applied surface loading corrections; average over all time series with >900 data points

in coastal regions or closely located to large lakes and might thus be affected by model generalizations.

Another way to assess the impact of loading corrections at the observation level is shown in Figure 7 for station POVE which was already assessed in Sect. 4.1. The amplitude spectra was derived based on the coordinate time series reduced for the estimated linear trend. Beside the clear decrease in the annual signal, signals are reduced for nearly all periods larger than 2 weeks (i.e. 26 cycles per year). For shorter time periods, signals are smaller than 1 mm and remaining noise might exceeds the loading effect. For the global perspective we computed an averaged spectra for all stations (Figure 8). Obviously, a significant reduction for signals at the annual and semi-annual periods with amplitudes of larger than 1 mm can be observed. Applying surface deformation models seems to remove signal for nearly all frequencies up to 50 cycles per year which correspond to a period of around week. In general, a signal reduction for periods between 10 and 30 days can be expected with correcting surface loading at the observation level. A more detailed study on this topic is underway but not discussed here.

Figure 9 shows the impact of applying surface loading models at the observation level on the annual signals contained in GNSS station height coordinate time series. To estimate the annual signals remaining in the GNSS network solution, Eqn. 1 was used to compute annual amplitudes and phases. Stations in South America and Central Asia show a significant decrease of the annual amplitudes which reaches up to 13 mm for the station POVE (see also Sect. 4.1). In total 83 % of the 178 amplitudes get smaller when correcting for non-tidal loading. Comparing to Figure 1 stations with large improvements are located mostly in regions with strong signals in terrestrial water storage like South America, Southeast Asia, or Western Canada or areas with large signals in atmospheric pressure like central Asia. Whereas only 13 % of the time series see slightly increased annual amplitudes (by maximal 1 mm), 4 % of the amplitudes increase by more than 1 mm. Stations with increasing amplitudes are mostly located in coastal areas like ASPA (American Samoa, +1.9 mm), COCO (Cocos Islands, +1.1 mm), MAS1 (Gran Canaria, +1.0 mm), PDEL (Acores, +1.3 mm), and YELL (Canada, +1.6 mm). The reason for the increased amplitude for the German station PTBB (Braunschweig) from 0.5 to 2.8 mm is so far unclear and differs significantly from other stations in Central Europe. Figure 10 shows the impact on station height coordinate repeatabilities by comparing the solution with applied models and the reference solution without applied models. Height coordinate repeatability values express the comparison of daily station coordinates dh_i with the combined solution dh_m and are computed as

$$\sigma_{hr} = \sqrt{\frac{1}{n-1}\sum_{i=1}^{n}(dh_i - dh_m)^2}. \qquad (4)$$

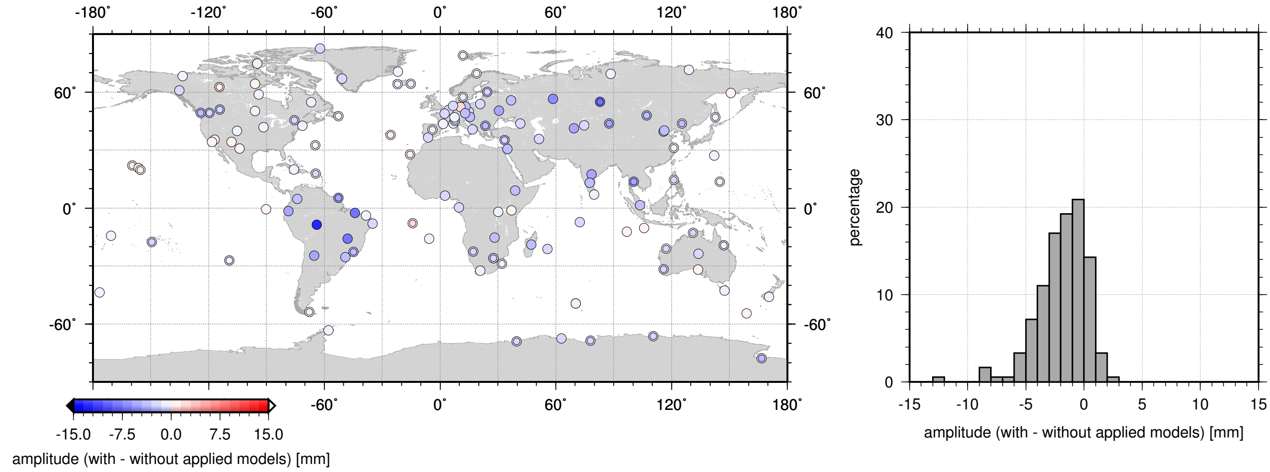

Fig. 9 Effect on annual amplitude of GNSS coordinate time series; differences *with - without applied models* are shown

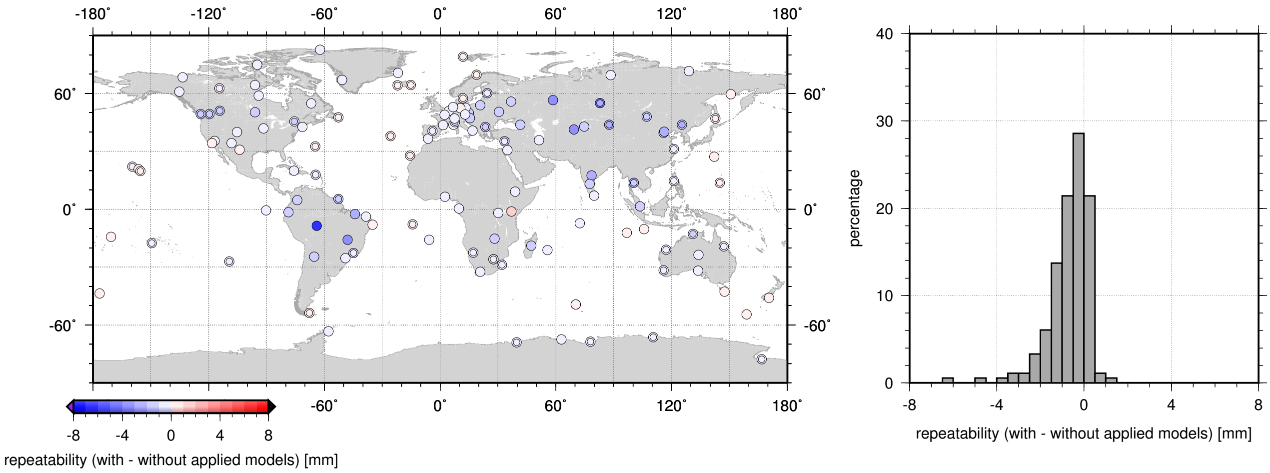

Fig. 10 Effect on the GNSS station height coordinate repeatability; differences *with - without applied models* are shown

In both cases velocities were subtracted from the time series. Overall a significant reduction of annual and inter-annual variability can be observed when correcting for surface loading. For nearly all stations, especially those located in South America and Central Asia, height coordinate repeatabilities decrease by several mm. Figure 10 shows the histogram of the differences of the station coordinate repeatabilities. Around 30 % of the time series differ by less than 0.5 mm whereas larger improvements of up to 7 mm can be found for 67 % of the time series. Whereas also many other stations show improvements of a few millimeters, a few stations located at island and in some cases located in coastal areas show slight degradation (in total 3 % of the stations). This effect is most probably related to complex coastal structure not adequately covered by global models (see Sect. 4.3).

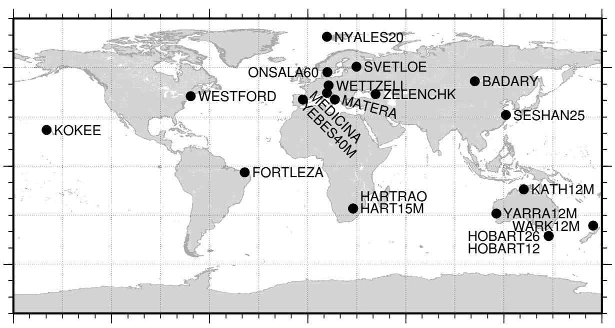

Fig. 11 Map of VLBI stations contained in the GNSS-VLBI comparison (see Table 3)

As described in Sect. 3 also VLBI data were processed with and without applying non-tidal loading models at the observation level. Table 3 provides annual amplitudes and phases of the height coordinate differences

Tab. 3 Annual amplitudes in height coordinate differences between GNSS and VLBI solutions (computed as $VLBI - GNSS$) with and without applied models; according to Eqn. 1; a map of all stations is provided in Figure 11

site	stations			without loading		with loading	
	VLBI	GNSS	time period	ampl [mm]	phase [°]	ampl [mm]	phase [°]
Badary	BADARY	BADG[a]	2011.69 - 2017.09	3.4±2.5	287.6±39.4	1.6±2.1	266.3±77.6
Fortaleza	FORTLEZA	BRFT	2008.01 - 2017.99	2.1±2.2	84.5±64.9	1.8±2.1	47.6±71.4
Hartebeesthoek	HART15M	HRAO	2014.58 - 2017.97	3.9±1.2	333.3±17.8	3.0±1.1	326.1±22.9
	HARTRAO	HARB	2011.93 - 2014.06	3.9±3.6	241.2±58.7	3.6±3.9	226.3±62.6
Hobart	HOBART26	HOB2	2010.59 - 2015.87	11.2±9.6	89.4±51.0	14.0±9.7	93.3±40.7
	HOBART12	HOB2	2010.77 - 2016.88	1.4±2.2	108.3±84.8	1.3±2.3	92.1±92.7
Katherine	KATH12M	KAT1[a]	2012.09 - 2016.80	4.9±2.7	97.6±30.0	2.7±1.8	80.3±37.8
Kokee Park	KOKEE	KOKB	2008.01 - 2017.99	3.3±1.3	263.3±23.2	2.4±1.3	273.8±32.5
Matera	MATERA	MATE	2008.91 - 2015.85	3.1±1.8	260.3±33.3	4.0±1.8	252.9±25.1
Medicina	MEDICINA	MEDI[a]	2012.48 - 2015.10	6.0±4.7	312.4±36.7	6.7±4.9	299.6±39.3
Ny-Ålesund	NYALES20	NYA2	2011.57 - 2016.49	2.9±1.4	283.0±29.2	3.9±1.4	281.3±21.7
Onsala	ONSALA60	ONSA	2008.04 - 2013.65	0.7±1.8	150.6±135.2	1.9±1.7	187.2±51.2
Sheshan	SESHAN25	SHAO	2011.47 - 2017.89	2.4±2.6	25.2±59.5	2.5±2.4	349.1±63.7
Svetloe	SVETLOE	SVTL[a]	2014.26 - 2017.07	2.9±3.8	350.6±73.1	2.6±3.8	245.1±86.6
Warkworth	WARK12M	WGTN[a]	2013.56 - 2016.57	3.4±3.4	280.0±60.8	4.4±3.4	304.6±47.0
Westford	WESTFORD	WES2	2010.09 - 2014.44	4.0±2.6	171.5±40.9	4.6±2.7	177.9±37.8
Wettzell	WETTZELL	WTZR	2011.30 - 2014.06	5.2±1.9	95.8±21.0	3.7±1.9	127.8±29.5
Yarragadee	YARRA12M	YAR2[a]	2013.48 - 2015.08	3.6±3.7	178.4±62.7	1.4±2.7	158.5±115.3
Yebes	YEBES40M	YEBE[a]	2008.70 - 2017.09	5.4±3.3	264.8±38.5	6.5±3.3	263.2±32.5
Zelenchukskaya	ZELENCHK	ZECK	2011.67 - 2017.78	4.8±2.1	63.0±26.9	3.5±2.1	66.3±36.6

[a] PPP results (a priori orbits without applied loading corrections)

between VLBI stations with longer time series and co-located GNSS receivers. Figure 11 shows the location of the VLBI stations listed in Table 3. The GNSS results are based on the network solution, only, if otherwise not available amplitudes were estimated from the PPP-based coordinates. For Hartebeesthoek and Hobart multiple co-locations are possible as the solutions contain for both stations two VLBI radio telescopes. Concepcion and Tsukuba are excluded here as their time series have multiple discontinuities caused by frequent earthquakes. Looking at technique-specific time series, VLBI amplitudes are in general smaller when models are applied (by up to 2 mm), increasing amplitudes occur only for `HOBART26` (0.4 mm), `SESHAN25` (1.0 mm) and `HART15M` (2.0 mm). Similar to GNSS, all amplitudes are smaller by up to 2.5 mm with models applied. Regarding the amplitude differences between GNSS and VLBI, GNSS amplitudes are mostly larger by 2-3 mm. The main reason for this offset might be the unconsidered behavior of GNSS monuments which can reach some mm (Yan et al, 2009). The amplitudes of the coordinate differences provided in Table 3 decrease at 11 of 20 co-locations considered here, on average the differences between VLBI and GNSS coordinates decrease by up to 2.2 mm. For the co-locations at the remaining sites the amplitudes increase by 0.6 to 1.2 mm, however also for these stations, the technique-specific amplitudes from VLBI and GNSS decrease by up to 1.5 mm when models are applied. If loading models are applied, the phase of the coordinate differences is shifted on average by 20°. Comparing the amplitude at co-located station of the same technique shows good agreement for GNSS (HARB-HRAO) with a difference of 0.4 and 0.1 mm for the solutions without and with applied corrections, respectively. Also the coordinate differences agree well for Hartebeesthoek with amplitudes of 3.0 and 3.6 mm (with models applied). For Hobart, Tasmania large amplitudes of more than 10 mm were estimated for the coordinate differences including the `HOBART26` telescope whereas the co-location with `HOBART12` shows amplitudes of 1.4 mm. The large amplitude found for `HOBART12` (technique-specific amplitudes exceed also 10 mm) might be caused by an issue with sthe local station equipment.

5.2 Satellite Orbits and Earth Orientation Parameters

In addition to the station coordinates also global parameters like GNSS satellite orbits and Earth rotation parameters are affected by loading deformation due to geophysical fluids. Correcting them consistently is possible only at the observation level. Previous studies based on atmospheric pressure loading by Dach et al (2011) and Sośnica et al (2015) showed that non-tidal loading has a small but persistent systematic impact on global parameters.

Comparing two satellite positions where loading cor-

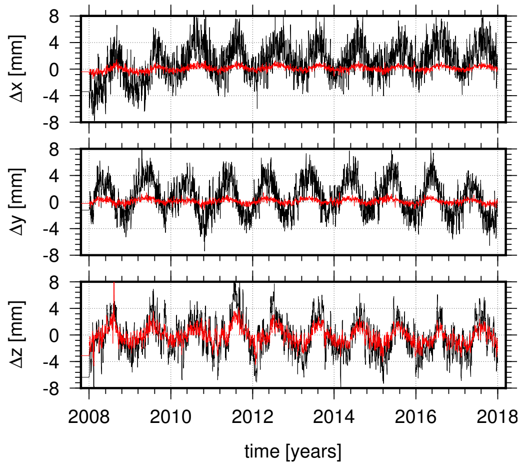

(a) Translation time series

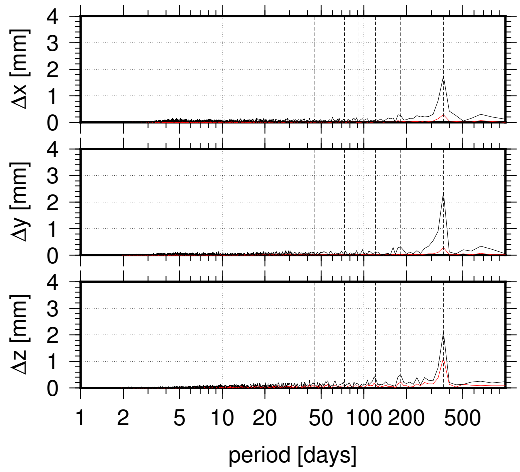

(b) Translations in spectra domain, annual and higher-order periods thereof are indicated with dashed lines

Fig. 12 Translations between GNSS satellite positions between orbits computed with and without applied non-tidal loading corrections (*red*) and translations between loadings provided in the CF and the CM frame (*black*)

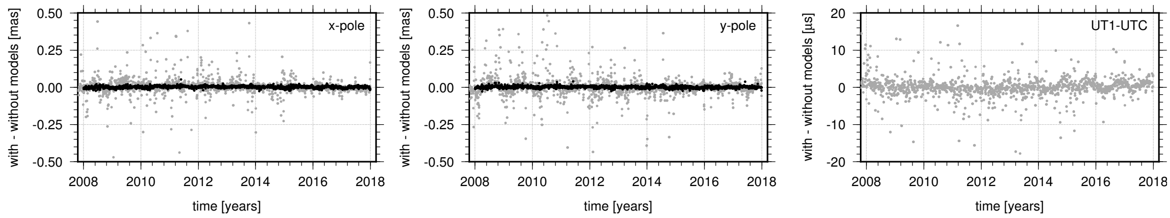

Fig. 13 Differences in x_P, y_P, and UT1-UTC estimates with and without applied surface loading corrections; for GNSS (*black*) and VLBI (*gray*)

rections are applied to only one orbit but not to the other show small differences of a few millimeters. In addition, small translations can be found as shown in Figure 12. The red curve shows translations in X- and Y-direction which are close to zero and amplitudes of up to 4 mm for the Z-component. Figure 12 shows also translations computed between the loading corrections given in CM and CF frames. These translations show a similar temporal behavior in the Z-component and amplitudes comparable to the orbit translations. Apparently, the difference between orbits determined with and without applied loading corrections is similar to mass re-distribution expressed by the different isomorphic frames. Considering the impact on the Keplerian elements, small but systematic differences of 2 mm in the semi-major axis can be found. High correlations between the variations of different satellites located close to each other as seen from the Earth (independent of block type, orbital plane, etc.) shows the impact of surface loading affecting the satellites in a similar way.

Figure 13 shows the difference between polar motion (x_p, y_p) and UT1-UTC estimated with and without applied loading models for GNSS and VLBI. For GNSS, the differences in x_p and y_p are around 0.02 mas which agrees to the results presented by Roggenbuck et al (2015). For VLBI, the differences are larger (up to 0.5 mas) and more scattered. The main reasons can be found in the smaller network size increasing the impact of loading corrections at certain sites and in the changing network geometry caused by the VLBI session definition. The latter can be seen especially in y_p differences before 2011. The differences in UT1-UTC are mostly below 3 µs with some larger values of up to 10 µs. Overall, the differences between VLBI results with and without applied loading corrections presented here is slightly larger than the results found by Roggenbuck et al (2015). Not shown here, the differences between GNSS and VLBI results are relatively small (below 1 mas), with smaller differences for solutions with applied loading corrections.

Despite the small changes in satellite orbits and Earth rotation parameters caused by non-tidal loading the consideration of surface loading for orbit and EOP determination is also important for a consistent GNSS processing. However, a pre-requisite for corrections at the parameter level is that the parameters are available in SINEX files. As already mentioned by Dach et al (2011), this is usually not the case for orbit parameters. Thus orbits cannot be corrected for surface loading on the parameter level.

6 Summary and Conclusions

Time-dependent mass variations in near-surface geophysical fluids cause significant load-induced deformations of the Earth's surface. Timeseries of conventionally processed space geodetic observations are currently dominated by those signals in particular at annual periods as revealed by a correlation analyses of the summed effect of surface deformations caused by atmospheric, oceanic, and terrestrial water mass changes with coordinate series from globally distributed space geodetic observing stations. In general, the comparison of annual signals and the computation of correlations between station coordinates and model-based deformations shows good agreement, especially for inland stations in South America, Eurasia, and parts of North America. For many stations, correlations of 0.5 and a good agreement in annual signals is documented. Stations located on small islands and in coastal areas generally show less agreement due to the limited spatial resolution of the considered global models and the rather large temporal variability of particularly the non-tidal ocean loading.

Accessibility of surface loading deformation models has been improved over the more recent years so that – somewhat redundant – model timeseries are now available from different globally distributed data providers. Moreover, since the ground segment of all space geodetic techniques is clearly and systematically affected by such deformations, we propose to carefully reconsider the IERS 2010 Conventions that abstained from recommending the application of a non-tidal surface deformation model at the observation level. Based on a GNSS network solution we found largely decreased annual amplitudes and improved repeatability in coordinate timeseries of almost all stations considered. Correcting non-tidal loading at the observation level shows in general reduced annual amplitudes for 83 % of the station coordinate time series and reduced coordinate repeatabilities by up to 6 mm for 78 % of the time series. As expected, largest improvements with a decrease of the annual signal by 13 mm are visible for the station POVE located in the Amazon basin. While comparing coordinate time series derived from VLBI and GNSS for co-located stations, a generally better agreement between coordinates from the two techniques is found when non-tidal loading models are consistently applied at the observation level.

We also found systematic translations in satellite orbits in particular in the Z-component of up to 2 mm amplitude at annual time-scales. For the VLBI network solution, we also note substantial changes in Earth orientation parameters that amount to up to 0.2 mas in polar motion, and 0.01 ms in UT1-UTC. We therefore suggest to recommend the application of non-tidal surface deformations at the observation level for future efforts aiming the estimatation of Earth orientation changes from VLBI networks, or the detection of transient tectonic or geomorphologic signals in coordinate timeseries of GNSS stations.

Acknowledgements The authors want to thank IGS and IVS for making publicly available GNSS and VLBI observations. All geophysical loading models evaluated herein can be accessed at `https://isdc.gfz-potsdam.de/esmdata/loading/`. We would also like to thank three anonymous reviewers for their assistance in evaluating this paper and their helpful recommendations.

Author contribution H.D., B.M., and S.G. defined the study. B.M. and K.B. processed the GNSS and VLBI data. All authors contributed to the analysis, interpretation, and discussion of the results. B.M. prepared the manuscript with major contributions from R.D., H.D., S.G., and K.B and inputs from all authors. All authors read and approved the final manuscript.

Data availablility statement All GNSS and VLBI data are available at IGS and IVS data centers, respectively. The ESMGFZ loading models are available at `http://isdc.gfz-potsdm.de/esmdata/loading`.

References

Altamimi Z, Rebischung P, Métivier L, Collilieux X (2016) ITRF2014: A new release of the International Terrestrial Reference Frame modeling non-linear station motions. J Geophys Res 121:6109–6131, DOI 10.1002/2016JB013098

Balidakis K, Nilsson T, Zus F, Glaser S, Heinkelmann R, Deng Z, Schuh H (2018) Estimating Integrated Water Vapor Trends From VLBI, GPS, and Numerical Weather Models: Sensitivity to Tropospheric Parameterization. J Geophys Res: Atmospheres 123(12):6356–6372, DOI 10.1029/2017JD028049

Bevis M, Alsdorf D, Kendrick E, Fortes LP, Forsberg B, Smalley R, Becker J (2005) Seasonal fluctuations in the mass of the Amazon River system and Earth's elastic response. Geophys Res Lett 32(16):L16,308, DOI 10.1029/2005GL023491

Blewitt G, Lavallee D (2002) Effect of annual signals on geodetic velocity. J Geophy Res 107(B7):ETG 9–1–ETG 9–11, 10.1029/2001JB000570

Böhm J, Werl B, Schuh H (2006) Troposphere mapping functions for GPS and VLBI from European Centre for medium-range weather forecasts operational analysis data. J Geophy Res 111(B2):B02,406, DOI 10.1029/2005JB003629

Böhm J, Heinkelmann R, Mendes Cerveira PJ, Pany A, Schuh H (2009) Atmospheric loading corrections at the observation level in VLBI analysis. J Geod 83(11):1107, DOI 10.1007/s00190-009-0329-y

Dach R, Böhm J, Lutz S, Steigenberger P, Beutler G (2011) Evaluation of the impact of atmospheric pressure loading modeling on GNSS data analysis. J Geod 85(2):75–91, DOI 10.1007/s00190-010-0417-z

van Dam T, Collilieux X, Wuite J, Altamimi Z, Ray J (2012) Non-tidal ocean loading: amplitudes and potential effects in GPS height time series. J Geod 86(11):1043–1057, DOI 10.1007/s00190-012-0564-5

Dill R (2008) Hydrological model LSDM for operational Earth rotation and gravity field variations, Scientific Technical Report STR, vol 369. GFZ

Dill R, Dobslaw H (2013) Numerical simulations of global-scale high-resolution hydrological crustal deformations. J Geophys Res 118(9):5008–5017, 10.1002/jgrb.50353

Dill R, Klemann V, Dobslaw H (2018) Relocation of River Storage From Global Hydrological Models to Georeferenced River Channels for Improved Load-Induced Surface Displacements. J Geophys Res: Solid Earth 123(8):7151–7164, DOI 10.1029/2018JB016141

Dobslaw H, Dill R, Grötzsch A, Brzezinski A, Thomas M (2010) Seasonal polar motion excitation from numerical models of atmosphere, ocean, and continental hydrosphere. J Geophys Res: Solid Earth 115(B10), DOI 10.1029/2009JB007127

Dobslaw H, Bergmann-Wolf I, Dill R, Poropat L, Thomas M, Dahle C, Esselborn S, König R, Flechtner F (2017) A new high-resolution model of non-tidal atmosphere and ocean mass variability for de-aliasing of satellite gravity observations: AOD1B RL06. Geophys J Int 211:263–269, DOI 10.1093/gji/ggx302

Dong D, Fang P, Bock Y, Cheng MK, Miyazaki S (2002) Anatomy of apparent seasonal variations from gps-derived site position time series. J Geophys Res 107(B4):ETG 9–1–ETG 9–16, DOI 10.1029/2001JB000573

Farrell W (1972) Deformation of the Earth by surface loads. Rev Geophys 10(3):761–797, DOI 10.1029/RG010i003p00761

Gegout P, Boy JP, Hinderer J, Ferhat G (2010) Modeling and Observation of Loading Contribution to Time-Variable GPS Sites Positions. In: Mertikas SP (ed) Gravity, Geoid and Earth Observation, Springer, Berlin, Heidelberg, pp 651–659

Jungclaus JH, Fischer N, Haak H, Lohmann K, Marotzke J, Matei D, Mikolajewicz U, Notz D, von Storch JS (2013) Characteristics of the ocean simulations in the Max Planck Institute Ocean Model (MPIOM) the ocean component of the MPI-Earth system model. J Adv Model Earth Sy 5(2):422–446, DOI 10.1002/jame.20023

Kennett BLN, Engdahl ER, Buland R (1995) Constraints on seismic velocities in the Earth from traveltimes. Geophys J Intern 122(1):108–124, DOI 10.1111/j.1365-246X.1995.tb03540.x

Lambeck K (1988) Geophysical Geodesy. Clarendon Oxford

Lyard F, Lefevre F, Letellier T, Francis O (2006) Modelling the global ocean tides: modern insights from FES2004. Ocean Dynamics 56(5-6):394–415, DOI 10.1007/s10236-006-0086-x

Männel B, Rothacher M (2017) Geocenter variations derived from a combined processing of LEO- and ground-based GPS observations. J Geod 91(8):933–944, doi:10.1007/s00190-017-0997-y

Nilsson T, Soja B, Karbon M, Heinkelmann R, Schuh H (2015) Application of Kalman filtering in VLBI data analysis. Earth, Planets and Space 67(1):136, DOI 10.1186/s40623-015-0307-y

Nordman M, Virtanen H, Nyberg S, Mkinen J (2015) Non-tidal loading by the Baltic Sea: Comparison of modelled deformation with GNSS time series. Geophys Res J 7:14 – 21, DOI doi:10.1016/j.grj.2015.03.002

Peltier A, Got JL, Villeneuve N, Boissier P, Staudacher T, Ferrazzini V, Walpersdorf A (2015) Long-term mass transfer at Piton de la Fournaise volcano evidenced by strain distribution derived from GNSS network. J Geophys Res 120(3):1874–1889, DOI 10.1002/2014JB011738

Petit G, Luzum B (2010) IERS Conventions (2010). IERS Technical Note 36. Verlag des Bundesamts für Kartographie und Geodäsie, Frankfurt am Main, iSBN 3-89888-989-6

Petrov L, Boy JP (2004) Study of the atmospheric pressure loading signal in very long baseline interferometry observations. J Geophys Res 109(B3):B03,405, DOI 10.1029/2003JB002500

Rabbel W, Schuh H (1986) The Influence of Atmospheric Loading on VLBI-Experiments. J Geophys 59(3):164–170

Ray R, Ponte R (2003) Barometric tides from ECMWF operational analyses. Ann Geophys 21(8):1897–1910

Roggenbuck O, Thaller D, Engelhardt G, Franke S, Dach R, Steigenberger P (2015) Loading-Induced Deformation Due to Atmosphere, Ocean and Hydrology: Model Comparisons and the Impact on Global SLR, VLBI and GNSS Solutions, Springer, Berlin, Heidelberg, pp 1–7. DOI 10.1007/1345_2015_214

Schuh H, Möhlmann L (1989) Ocean Loading Station Displacements Observed by VLBI. Geophys Res Lett 16(10):1105 – 1108

Sośnica K, Jäggi A, Meyer U, Thaller D, Beutler G, Arnold D, Dach R (2015) Time variable Earth's gravity field from SLR satellites. J Geod pp 1–16, DOI 10.1007/s00190-015-0825-1

Steigenberger P, Böhm J, Tesmer V (2009) Comparison of GMF/GPT with VMF1/ECMWF and implications for atmospheric loading. J Geod 83(10):943, DOI 10.1007/s00190-009-0311-8

Tregoning P, van Dam T (2005) Effects of atmospheric pressure loading and seven-parameter transformations on estimates of geocenter motion and station heights from space geodetic observations. J Geophys Res 110(B3):n/a–n/a, DOI 10.1029/2004JB003334, b03408

Williams SDP, Penna NT (2011) Non-tidal ocean loading effects on geodetic GPS heights. Geophysical Research Letters 38(9), DOI 10.1029/2011GL046940

Yan T, Lim S, Rizos C (2009) Performance analysis of real-time GNSS data distribution over the internet. Proceedings of SSC2009, Adelaide, Australia 28:491–502

Zus F, Dick G, Douša J, Heise S, Wickert J (2014) The rapid and precise computation of GPS slant total delays and mapping factors utilizing a numerical weather model. Radio Science 49(3):207–216, DOI doi:10.1002/2013RS005280